Theory of spin wave modes in tangentially magnetized thin cylindrical dots: A variational approach

R. Zivieri
Dipartimento di Fisica, Università di Ferrara, Via Saragat 1, I-44100 Ferrara, Italy

R. L. Stamps
Department of Physics, University of Western Australia, Nedlands, WA 6907, Australia

(Received 6 August 2005; revised manuscript received 8 February 2006; published 19 April 2006; corrected 28 April 2006)

We present a theoretical study of the quantized spin wave spectrum in tangentially magnetized cylindrical thin magnetic dots. Low-energy spin waves in magnetic dots may be subdivided into four families: Damon-Eshbach like, backward like, mixed, and end modes. Frequencies and mode profiles are found using a variational approach based on carefully chosen trial functions. The variational method has the advantage that it can be used for large dots that are not practical to treat using numerical finite-element methods. Results for small dots generated using the variational method compare well with micromagnetic results. The variational method is demonstrated with an analysis of data obtained from experimental Brillouin light scattering data from saturated thin cylindrical Permalloy dots. Our approach allows for the definition of parameters describing important contributions to the spin wave energies. As an example, we show that a variational parameter ϵ provides a measure of spin wave localization near the dot border for one class of modes.

DOI: 10.1103/PhysRevB.73.144422 PACS number(s): 75.30.Ds, 75.75.+a

I. INTRODUCTION

The low-frequency dynamical properties of magnetic nanostructures can be strongly modified by the geometrical structure and are important to understand in terms of thermal stability, field- and current-induced switching, and fundamental studies of interface and surface magnetism. A great deal of experimental work using Brillouin light scattering (BLS) has demonstrated discretization effects due to the lateral confinement of nanostructured materials of different shapes.[1–3] Consequently, great attention has also been devoted to theoretical models developed to explain quantized spin dynamics in magnetic nanostructures.

The low-energy spin wave excitations can involve substantial contributions from magnetostatic energies. Magnetostatic interactions in dynamics are nonlocal and can be difficult to treat when attempting accurate predictions of spin wave frequencies in constrained geometries. One common approach is to use numerical micromagnetics to solve finite-difference equations in real-time micromagnetics. This approach suffers from severe limitations in structure dimensions that can be practically dealt with and also from more subtle issues related to spurious symmetries introduced by discretization.

Analytical methods can provide important physical insights and are capable in principle of providing useful techniques for realistic sized structures. A serious challenge is to find practical methods of approximating the nonlocal magnetostatic interactions while simultaneouously providing eigenfrequencies with precision sufficient to match the fine resolutions capable with state-of-the-art inelastic scattering and resonance methods. For example, in the case of thin magnetic stripes an important progress has been made[4] in obtaining a boundary condition directly from the dipolar integral operator. Furthermore, the wave-number quantization obtained from the boundary condition in the limit of small stripe aspect ratio gives numerical results very close to that proposed through the empirical formula for Permalloy wires of Ref. 5 for the modes with a small number of nodes.

The first studies of the spin dynamics in infinite axially magnetized circular cylinders were performed by Fletcher and Kittel[6] and later on in axially magnetized yttrium iron garnet (YIG) rods by Abe and Ikushima.[7] More recently, a theory of the dipole-exchange spin waves in axially magnetized cylindrical ferromagnetic nanowires has been formulated taking also into account the dipolar interaction between arrays of wires.[8,9] The generalization of this theory to rectangular and elliptical axially magnetized nanowires has been done in Ref. 10. Moreover, very recent studies have also been carried out to successfully describe the dynamics of interacting perpendicularly magnetized cylindrical dots both experimentally by means of *X*-band ferromagnetic resonance (FMR) and theoretically.[11,12]

Despite these advances, significant difficulties have been encountered for the problem of cylindrical dots in the in-plane saturated configuration. In order to partially overcome these difficulties it has been in a first instance supposed that the dynamic magnetization at the border was unpinned.[13,14] Subsequently, studying magnetic thin stripes it has been found that the pinning parameter depends on the geometry and that the pinning effect is of purely dipolar nature.[4]

To the best of our knowledge there are no theoretical studies which describe in a unitary way the normal modes in saturated circular dots fulfilling boundary conditions in the presence of dynamic pinning including exchange contributions that are valid when rotational symmetry is lacking due to in-plane saturation. The purpose of this paper is to present a variational theory which overcomes these limitations and is able to encompass the most important features of spin excitations inside a cylindrical dot based on trial eigenfunctions

for each family of spin modes. In order to construct suitable trial functions for each family of normal modes, we note that the dynamical magnetization for a given mode in a confined system like a dot should be a superposition of normal modes oscillating at different angles with respect to the in-plane direction of the applied field **H**. This analysis is physically consistent and not restrictive if we consider one normal mode in the form of a stationary wave characterized by an in-plane wave-number with prevalent components along either the x or y axis (k_x or k_y) or along both x and y axes, but also with a radial character implicit in the Bessel function expansion. Our solution is written as a truncated expansion in cylindrical Bessel functions of increasing orders. We will justify in the following this approximation that leads to a consistent simplification of the model allowing us to express the trial eigenfunction in a simple form. As we will demonstrate, this approach provides more accurate solutions than previous studies where an expansion in a series of Bessel functions where the radial dependence is separated from the azimuthal dependence or a film plane wave satisfying radial boundary conditions in a confined system were taken as approximate eigenfunctions.[13,14] Furthermore, the agreement of the calculated frequencies of the most representative modes with the available experimental ones results as a whole very good.

Concerning the demagnetizing field calculation the present work differs from that of Ref. 14 because there only the averaged radial dependence of the in-plane demagnetizing factor is calculated from a generalization to the in-plane case of the Joseph-Schlömann formalism.[15] In this paper we use a different method entirely to calculate analytically both the radial and azimuthal dependence and thereby obtain accurate results for all families of allowed modes.

Our variational approach predicts the existence of end modes observed and widely discussed in thin stripes and rectangular and cylindrical dots.[13,14,16] These excitations are classified as end modes in a recent micromagnetic calculation based on a dynamical matrix approach applied to dots of different shapes.[17,18] Up to now frequencies of these modes have been derived by assuming a potential-well resonance quantization condition that has been applied to different geometries. Our method provides a consistent analytical theory for these modes in cylindrical dots and a localization parameter.

The paper is organized as follows: in Sec. II the model is presented. Section II B discusses the dynamics of each set of modes and their corresponding boundary conditions. We discuss the results of the present model applied to Permalloy dots in Sec. III. In Sec. IV a summary of the results obtained in the present work together with some interesting open questions is presented.

II. VARIATIONAL THEORY

In this section a variational theory for the calculation of the quantized spectrum of spin wave modes in a saturated cylindrical dot is presented. Our results are applicable to dot arrays in the case where the interdot distance is at least equal to or larger than the dot diameter $2R$ and is also larger than the dot thickness L so that dipolar coupling between dots can be neglected. Moreover, since we deal with thin dots, we neglect the dependence of the dynamic magnetization components from the wave-number component perpendicular to the dot surface. We also do not include into the Hamiltonian the magnetocrystalline anisotropy, because we study polycrystalline dots. We also neglect the shape anisotropy. We consider thin dots of aspect ratio $\beta=\frac{L}{R}$ less than 0.25 and assume that the magnetization profile across the dot thickness is uniform. Errors that could be introduced by this assumption are discussed in our analysis of experimental data taken from Permalloy dots.

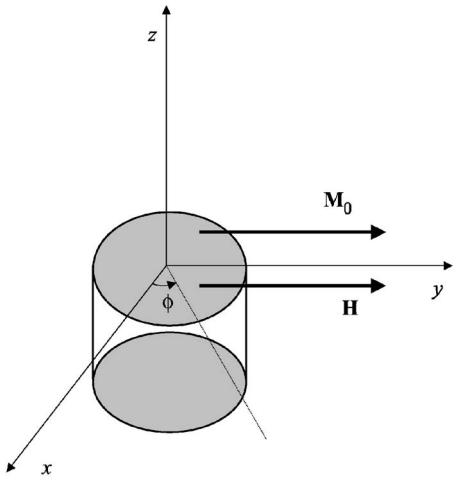

FIG. 1. Schematic representation of the system. $\mathbf{M}_0$: static magnetization on the x-y plane and parallel to the y axis. **H**: applied field along the y axis.

We choose a coordinate system with the z axis normal to the dot surface and the static magnetization $\mathbf{M}_0$ aligned along the y axis and assumed uniform for small aspect ratio. A schematic representation of the system is given in Fig. 1. The total magnetization is expressed as a sum of a static and a dynamic part—viz., $\mathbf{M}(\mathbf{r},t)=\mathbf{M}_0+\mathbf{m}(\mathbf{r},t)$. Neglecting second-order dynamic terms, the linearized equations of motion are

$$-\frac{1}{\gamma}\frac{d\mathbf{m}(\mathbf{r},t)}{dt}=\mathbf{m}(\mathbf{r},t)\times\mathbf{H}_s^{\mathrm{eff}}(\mathbf{r})+\mathbf{M}_0\times\mathbf{h}_d^{\mathrm{eff}}(\mathbf{r},t). \quad (1)$$

γ is the gyromagnetic ratio. The static internal field to the first order[15] may be written as $\mathbf{H}_s^{\mathrm{eff}}(\mathbf{r})=\mathbf{H}+\mathbf{H}_s^{(1)}(\mathbf{r})$. **H** is the external field, $\mathbf{H}_s^{(1)}(\mathbf{r})$ is the first-order static demagnetizing field, and the dynamic effective field is $\mathbf{h}_d^{\mathrm{eff}}(\mathbf{r},t)=\mathbf{h}_{\mathrm{exch}}(\mathbf{r},t)+\mathbf{h}_d(\mathbf{r},t)$. $\mathbf{h}_{\mathrm{exch}}(\mathbf{r},t)=\alpha\nabla^2\mathbf{m}(\mathbf{r},t)$ is the dynamic nonuniform exchange field where $\alpha=\frac{2A}{M_s^2}$ is the exchange constant and A is the exchange stiffness constant. $\mathbf{h}_d(\mathbf{r},t)$ is the dynamic dipolar field.

The dynamic magnetization components are m_x and m_z and are assumed to vary in time according to $\exp(-i\omega t)$. Defining $\Omega=\omega/\gamma$, the linearized equations of motion are written as

$$[H+H_s^y(\mathbf{r})-\alpha M_s\nabla^2]m_x(\mathbf{r})-M_s h_d^x(\mathbf{r})=i\Omega m_z(\mathbf{r}), \quad (2)$$

$$[H + H_s^y(\mathbf{r}) - \alpha M_s \nabla^2] m_z(\mathbf{r}) - M_s h_d^z(\mathbf{r}) = -i\Omega m_x(\mathbf{r}). \quad (3)$$

$H_s^y(\mathbf{r})$ is the y component of the first-order demagnetizing field, and $M_s = |\mathbf{M}_0|$ is the saturation magnetization.

We calculate the first-order static demagnetizing field as an integral over the static magnetization:

$$\mathbf{H}_s^{(1)}(\mathbf{r}) = \int_{V'} d^3\mathbf{r}' \hat{\Gamma}(\mathbf{r}, \mathbf{r}') \mathbf{M}_0. \quad (4)$$

$\hat{\Gamma}(\mathbf{r}, \mathbf{r}') = -(\nabla_{\mathbf{r}})(\nabla_{\mathbf{r}'}) \frac{1}{|\mathbf{r}-\mathbf{r}'|}$ is the magnetostatic tensorial Green function in the cylindrical system $(\alpha, \beta = \rho, \phi, z)$, and the integration is over the dot volume V'. The first-order dynamic demagnetization field has a similar form

$$\mathbf{h}_d(\mathbf{r}, t) = \int_{V'} d^3\mathbf{r}' \hat{\Gamma}(\mathbf{r}, \mathbf{r}') \mathbf{m}(\mathbf{r}', t). \quad (5)$$

Averaging $\hat{\Gamma}(\mathbf{r}, \mathbf{r}')$ over z and z' we define a radial Green function

$$\hat{G}(\boldsymbol{\rho}, \boldsymbol{\rho}') = -\frac{1}{L} \int_{-L}^{0} dz \int_{-L}^{0} dz' (\nabla_{\mathbf{r}})(\nabla_{\mathbf{r}'}) \frac{1}{|\mathbf{r} - \mathbf{r}'|}. \quad (6)$$

The first-order in-plane coordinate-dependent static demagnetizing field is then written as an integral over the dot surface S':

$$\mathbf{H}_s^{(1)}(\boldsymbol{\rho}) = \int_{S'} d^2\boldsymbol{\rho}' \hat{G}(\boldsymbol{\rho}, \boldsymbol{\rho}') \mathbf{M}_0. \quad (7)$$

The in-plane coordinate-dependent demagnetizing tensor is defined as

$$\hat{N}(\boldsymbol{\rho}) = -\frac{1}{4\pi} \int_{S'} d^2\boldsymbol{\rho}' \hat{G}(\boldsymbol{\rho}, \boldsymbol{\rho}'). \quad (8)$$

The magnetostatic Green function average over z and z' we make decouples the in- and out-of-plane components so that the demagnetization tensor has the form

$$\hat{N}(\boldsymbol{\rho}) = \begin{bmatrix} N_{xx} & N_{xy} & 0 \\ N_{yx} & N_{yy} & 0 \\ 0 & 0 & N_{zz} \end{bmatrix}. \quad (9)$$

Using Eqs. (8) and (9), the first-order static demagnetizing field is

$$\mathbf{H}_s^{(1)}(\boldsymbol{\rho}) = -4\pi[(N_{xx} M_0^x + N_{xy} M_0^y)\hat{i} + (N_{yx} M_0^x + N_{yy} M_0^y)\hat{j} + N_{zz} M_0^z \hat{k}], \quad (10)$$

where M_0^x, M_0^y, and M_0^z are the three components of the static magnetization, and $\hat{i}$, $\hat{j}$, and $\hat{k}$ are unit vectors along the x, y, and z axes, respectively.

Under the assumption that $|M_0^z| \ll M_s$ valid for thin dots, the z-component of the static demagnetizing field $H_s^z(\boldsymbol{\rho})$ may be neglected. Instead, due to the stray dipolar field along the x direction, we should take into account both $H_s^x(\boldsymbol{\rho})$ and $H_s^y(\boldsymbol{\rho})$, the x and the y components of the first-order static demagnetizing field, respectively. The two components are expressed as

$$H_s^x(\boldsymbol{\rho}) = -4\pi M_s N_{xy}(\boldsymbol{\rho}) \quad (11)$$

and

$$H_s^y(\boldsymbol{\rho}) = -4\pi M_s N_{yy}(\boldsymbol{\rho}), \quad (12)$$

assuming that the system is uniformly magnetized along the y direction—i.e., $|M_0^x| \ll M_s$ and $|M_0^y - M_s| \ll M_s$—i.e., $|M_0^y| \simeq M_s$. Under this approximation we neglect border effects which could induce a reorientation of the static magnetization near the border perpendicular to the y direction. This assumption is valid for materials where the exchange length is large. Note that only the H_s^y component of the static demagnetizing field enters into the torque components of the linearized equations of motion [cf. Eqs. (2) and (3)].

We now perform a Fourier expansion in cylindrical coordinates in order to calculate the demagnetizing tensor components. Using the expansion

$$\frac{1}{|\mathbf{r} - \mathbf{r}'|} = \sum_{m=-\infty}^{\infty} \int_0^{\infty} dk e^{im(\phi - \phi')} J_m(k\rho) J_m(k\rho') e^{-k|z-z'|}, \quad (13)$$

we calculate the averaged magnetostatic Green function given in Eq. (6) which is in turn substituted into Eq. (8). In this calculation it is convenient to write the two required tensor components G_{xy} and G_{yy} in a cylindrical coordinate system as

$$G_{xy} = G_{\rho\rho} \cos\phi \sin\phi' + G_{\rho\phi} \cos\phi \cos\phi' - G_{\phi\rho} \sin\phi \sin\phi' - G_{\phi\phi} \sin\phi \cos\phi' \quad (14)$$

and

$$G_{yy} = G_{\rho\rho} \sin\phi \sin\phi' + G_{\rho\phi} \sin\phi \cos\phi' + G_{\phi\rho} \cos\phi \sin\phi' + G_{\phi\phi} \cos\phi \cos\phi', \quad (15)$$

where $G_{\rho\rho}$, $G_{\rho\phi}$, $G_{\phi\rho}$, and $G_{\phi\phi}$ are the components of the z- and z'-averaged Green function tensor $G_{\alpha\beta}(\boldsymbol{\rho}, \boldsymbol{\rho}')$ in the cylindrical system $(\alpha, \beta = \rho, \phi, z)$.

Inserting these into G_{xy} and G_{yy}, substituting into Eq. (8), and integrating over $d^2\boldsymbol{\rho}'$ provides explicit definitions for the demagnetizating tensor components. In particular, we have

$$N_{xy}(\rho, \phi) = \frac{R}{2} \left[\int_0^{\infty} dk \chi(kL) J_1(kR) J_0(k\rho) \sin 2\phi \right] \quad (16)$$

and

$$N_{yy}(\rho, \phi) = R \left[\int_0^{\infty} dk \chi(kL) J_1(kR) J_0(k\rho) \sin^2\phi + \int_0^{\infty} dk \chi(kL) J_1(kR) \frac{J_1(k\rho)}{k\rho} \cos 2\phi \right]. \quad (17)$$

Note that the function $\frac{2}{k}\chi(kL)$ with $\chi(kL) = 1 - \frac{1 - e^{-kL}}{kL}$ is the result of the average over z and z'. For the calculation of the integrals given in Eqs. (16) and (17) see Appendix A.

In Fig. 2 we show the profile of the $N_{yy}(\rho, \phi)$ calculated with Eq. (17) [see Appendix A, Eqs. (A2)–(A10) for the details of the calculation]. The demagnetizing tensor compo-

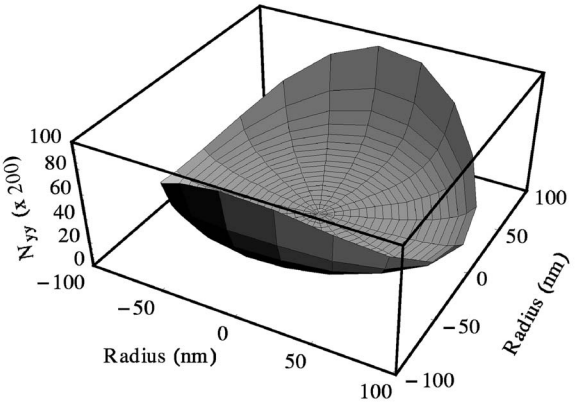

FIG. 2. Profile of the demagnetizing tensor component N_{yy} on the x-y plane calculated using Eq. (17) for a dot of $R=100$ nm and $L=15$ nm.

nent has a strong inhomogeneity throughout the dot, especially along the direction of the saturation magnetization (y direction). It has a minimum in the center of the dot and a maximum on the boundary along the y direction $(\phi=\frac{\pi}{2},\frac{3}{2}\pi)$. Along the x direction $(\phi=0,\pi)$ the factor has a small curvature. The nonuniformity of $N_{yy}(\rho,\phi)$ strongly affects the mode frequencies with the result that each mode feels a different static demagnetizing factor. This is important for an accurate understanding of the low frequency properties of each mode.

Since Eqs. (2) and (3) contain the differential operator of the second order, an additional first-order boundary condition is necessary to determine the dynamic magnetization. The condition is applied on the dot lateral surface $\rho=R$ and gives the wave-number k quantization. We neglect the z dependence of the dynamic magnetization, because we consider here thin dots. On this basis the radial boundary condition may be written for the two dynamic magnetization components as

$$\rho\ \frac{\partial m_x(\boldsymbol{\rho})}{\partial n}+p_x m_x(\boldsymbol{\rho})\bigg|_{\rho=R}=0, \tag{18}$$

$$\rho\ \frac{\partial m_z(\boldsymbol{\rho})}{\partial n}+p_z m_z(\boldsymbol{\rho})\bigg|_{\rho=R}=0, \tag{19}$$

where $\frac{\partial}{\partial n}$ denotes the partial derivative in the direction of a unit vector $\hat{n}$ which points outward and is normal to the lateral surface of the dot and $p_x(p_z)$ is the pinning parameter on the boundary for the $m_x(m_z)$ component, respectively.

In general we expect some degree of mode pinning at the boundary and the degree of pinning is determined by a competition between the magnetostatic energy on the dot lateral surface and the exchange energy. Due to the presence of a static dipolar field on the border, we may attribute a pinning parameter also to the m_z component. Recent studies for cylindrical geometries assume no pinning as a simplifying assumption;[13,14] however, with our theory we are able to provide and evaluate an expression for a pinning parameter p.

We first write the exchange boundary conditions for cylindrical dots in analogy to the case of saturated magnetic films Rado-Weertmann exchange boundary conditions.[19,20] In order to do this we treat the surface dipolar energy at the dot boundary, which is responsible for a surface-torque density other than ferromagnetic exchange, like a surface anisotropy energy. We require the associated surface-torque density to vanish at the boundary:

$$\mathbf{M}\times\left(\nabla_{\mathrm{M}}E_{\mathrm{s}}(\boldsymbol{\rho})+\nabla_{\mathrm{m}}E_{\mathrm{d}}(\boldsymbol{\rho},\boldsymbol{\rho}')-\frac{2A}{M_s^2}\frac{\partial\mathbf{m}(\boldsymbol{\rho})}{\partial n}\right)\bigg|_{\rho,\rho'=R}=0, \tag{20}$$

where $E_s(\boldsymbol{\rho})$ is the coordinate-dependent in-plane static dipolar energy per unit surface. $E_{\mathrm{d}}(\boldsymbol{\rho},\boldsymbol{\rho}')$ may be interpreted as the nonlocal in-plane dynamic dipolar energy per unit surface, and $\frac{2A}{M_s^2}\frac{\partial\mathbf{m}(\boldsymbol{\rho})}{\partial n}$ is related to the dynamic exchange surface energy. Equation (20) can then be expressed in terms of surface torque components as

$$\left(\frac{\partial}{\partial M_s}E_{\mathrm{s}}(\rho,\phi)m_z(\rho,\phi)-M_s\frac{\partial}{\partial m_z}E_{\mathrm{d}}(\rho,\rho',\phi,\phi')+\frac{2A}{M_s}\frac{\partial m_z(\rho,\phi)}{\partial\rho}\right)\bigg|_{\rho,\rho'=R}=0 \tag{21}$$

and

$$\left(\frac{\partial}{\partial M_s}E_{\mathrm{s}}(\rho,\phi)m_x(\rho,\phi)-M_s\frac{\partial}{\partial m_x}E_{\mathrm{d}}(\rho,\rho',\phi,\phi')+\frac{2A}{M_s}\frac{\partial m_x(\rho,\phi)}{\partial\rho}\right)\bigg|_{\rho,\rho'=R}=0. \tag{22}$$

We restrict ourselves to Eq. (22) where also $E_{\mathrm{d}}(\rho,\rho',\phi,\phi')$ gives a nonvanishing contribution. Since the static dipolar energy per unit volume at the dot boundary is $U_{\mathrm{s}}(\rho,\phi)|_{\rho=R}=2\pi M_s^2 N_{yy}(R,\phi)$, we have that $E_{\mathrm{s}}(\rho,\phi)|_{\rho=R}=\pi R M_s^2 N_{yy}(R,\phi)$. The nonlocal part is $E_{\mathrm{d}}(\rho,\rho',\phi,\phi')|_{\rho,\rho'=R}$ which may be expressed as

$$E_{\mathrm{d}}(\rho,\rho',\phi,\phi')|_{\rho,\rho'=R}=\frac{\displaystyle\int_{-L}^{0}dz\int_{-L}^{0}dz'\frac{1}{|\mathbf{r}-\mathbf{r}'|}\mathbf{m}(\rho,\phi)\cdot\hat{n}\mathbf{m}(\rho',\phi')\cdot\ \hat{n}|_{\rho=R,\rho'=R}}{4\pi\beta}, \tag{23}$$

where $(\mathbf{r}-\mathbf{r}')^2=\rho^2+\rho'^2-2\rho\rho'\cos(\phi-\phi')+(z-z')^2$.

We can therefore write the associated quantities related to the effective boundary fields as

$$\frac{\partial}{\partial M_s} E_s(\rho,\phi)\big|_{\rho=R} = 2\pi R M_s N_{yy}(R,\phi) \tag{24}$$

and

$$\frac{\partial}{\partial m_x} E_d(\rho,\rho',\phi,\phi')\big|_{\rho,\rho'=R} = \frac{1}{4\pi}\left[R\cos\phi\cos\phi' \left(\int_{-L}^{0} dz \frac{1}{|\mathbf{r}'-\mathbf{r}|}\int_{-L}^{0} dz' + \int_{-L}^{0} dz' \frac{1}{|\mathbf{r}-\mathbf{r}'|}\int_{-L}^{0} dz \right)\right|_{\rho=R,\rho'=R}\right] m_x(R,\phi). \tag{25}$$

Integrating over ϕ and ϕ' the quantity between square brackets in Eq. (25), which may be interpreted as a dynamic demagnetizing factor on the border, and substituting the second member of Eq. (24) together with the result of the integration of Eq. (25) into Eq. (22) we define our pinning parameter as the following:

$$p(\phi,\beta) = p_s(\phi,\beta) + p_d(\beta), \tag{26}$$

where

$$p_s(\phi,\beta) = \frac{1}{2}\frac{R^2}{l_0^2} N_{yy}(R,\phi,\beta) \tag{27}$$

is the contribution to p related to the static demagnetizing field. $l_0=(A/2\pi M_s^2)^{\frac{1}{2}}$ is the reduced exchange length and

$$p_d(\beta) = -\frac{1}{2}\frac{R^2}{l_0^2} I_{p_d}(\beta) \tag{28}$$

is the dynamic part of p arising from the dynamic dipolar energy. Note that to obtain $p_d(\beta)$ from Eq. (25) with the same prefactor $-\frac{1}{2}\frac{R^2}{l_0^2}$ of p_s (apart from the sign) we have not integrated over the azimuthal angle $m_x(R,\phi)$. The exact approach would be to leave the dependence on ϕ in p_d and to average it in the boundary condition given in the following; however, we have numerically checked that it would lead substantially to the same wave-number numerical values as those obtained with the above approximated approach.

We have also included the explicit dependence on the aspect ratio β in N_{yy}. The calculation of $N_{yy}(R,\phi,\beta)$ and $I_{p_d}(\beta)$ is given in Appendix B. We have found that here pinning minimizes the dipolar energy at the surface as for the case of thin magnetic stripes[4] where competition from exchange has been neglected. The pinning parameter is found to depend on the aspect ratio $\beta=L/R$ and the azimuthal coordinate ϕ, but does not depend explicitly on the mode number n. Furthermore, from the numerical calculations it is straightforward to show that the dynamic part contribution p_d is only a small correction to the static value. Finally, p becomes large at large R (or decreasing the aspect ratio β). This is analogous to the case of thin stripes where pinning is largest for wide wires. The same conclusions concerning the pinning of the m_x component may be drawn using the boundary condition of Eq. (21) on the m_z component assuming the same pinning effects even if in principle for the latter the dynamic contribution to the pinning rigorously vanishes.

We treat the angular dependence of the boundary conditions by averaging over the ϕ angle. This average allows us to take into account the contribution of the azimuthal dependence of both the mode eigenfunctions and of the pinning parameter giving a correction to the wave-number quantization obtained using unidirectional boundary conditions. Furthermore, in this way it is possible to single out the radial character of the spin modes that is intrinsic in their Bessel series representation. The average is defined by

$$\frac{1}{\phi''-\phi'}\int_{\phi'}^{\phi''} d\phi \left(\rho\frac{\partial m_x^n(\rho,\phi)}{\partial\rho} + p(\phi,\beta) m_x^n(\rho,\phi)\right)\Bigg|_{\rho=R} = 0, \tag{29}$$

where n gives the number of nodes throughout the dot. On the basis of what we have stated above about the pinning we assume the same wave-number quantization also for the m_z component. At this stage we differentiate between symmetric (S) and antisymmetric (AS) spin modes with respect to a plane perpendicular to the dot surface. For S modes we take $\phi'=0$ and $\phi''=2\pi$. The limits of integration of AS modes are specified in Sec. II B for each family of modes.

It is known that an in-plane magnetization in a disk breaks the axial symmetry of the Walker equation[21] valid for an axially symmetric spheroid inducing a strongly in-plane coordinate-dependent static demagnetizing field. Even neglecting in Eqs. (2) and (3) the dynamic dipolar field, in the presence of a broken symmetry an analytical solution of the radial part of Eqs. (2) and (3) does not exist, because it is not possible in a cylindrical dot in the saturated state to single out the azimuthal dependence in the demagnetizing tensor components and to separate it from the radial dependence.

Nevertheless, averaging the demagnetizing field over the dot surface and neglecting the perturbation introduced by the dynamic dipolar field, analytical forms for eigenfunctions of the effective field operator exist and one can show that they take the form of stationary waves.

We implement our variational approach by first constructing suitable trial functions based on these eigenfunctions. Given a trial eigenfunction, a frequency Ω functional is constructed as follows. First, we multiply together the two linearized equations of motion [cf. Eqs. (2) and (3)] rewritten assuming only an in-plane dependence for the dynamic magnetization. The resultant equation is then multiplied on the left by $m_x^{*n'}(\boldsymbol{\rho})$ and $m_z^{*n'}(\boldsymbol{\rho})$ and followed by an integration over $d^2\boldsymbol{\rho}$. The result is

$$\Omega = \left[\frac{\int d^2\boldsymbol{\rho} m_x^{*n'}(\boldsymbol{\rho})[H + H_{\mathrm{dem}}^y(\boldsymbol{\rho}) - \alpha M_s \nabla^2] m_x^n(\boldsymbol{\rho}) - M_s \int d^2\boldsymbol{\rho} m_x^{*n'}(\boldsymbol{\rho}) h_x^n(\boldsymbol{\rho})}{\int d^2\boldsymbol{\rho} m_x^{*n'}(\boldsymbol{\rho}) m_x^n(\boldsymbol{\rho})} \right]^{1/2} \times \left[\frac{\int d^2\boldsymbol{\rho} m_z^{*n'}(\boldsymbol{\rho})[H + H_{\mathrm{dem}}^y(\boldsymbol{\rho}) - \alpha M_s \nabla^2] m_z^n(\boldsymbol{\rho}) - M_s \int d^2\boldsymbol{\rho} m_z^{*n'}(\boldsymbol{\rho}) h_z^n(\boldsymbol{\rho})}{\int d^2\boldsymbol{\rho} m_z^{*n'}(\boldsymbol{\rho}) m_z^n(\boldsymbol{\rho})} \right]^{1/2}. \tag{30}$$

Next we define the integrals appearing in Eq. (30).

(i) Normalization integral

$$N_i^{nn'} = \int d^2\boldsymbol{\rho} m_i^{n'}(\boldsymbol{\rho}) m_i^n(\boldsymbol{\rho}) = N_i^n \delta_{nn'}.$$

(ii) Exchange integral

$$E_i^{nn'} = \bar{E}_i^{nn'} / N_i^{nn'},$$

(iii) Static demagnetizing integral

$$D_i^{nn'} = \bar{D}_i^{nn'} / N_i^{nn'},$$

(iv) Dynamic demagnetizing integral

$$d_i^{nn'} = \bar{d}_i^{nn'} / N_i^{nn'} \text{ with } \bar{d}_i^{nn'} = \int d^2\boldsymbol{\rho} m_i^{*n'}(\boldsymbol{\rho}) h_i^n(\boldsymbol{\rho}) \text{ and } h_i^n(\boldsymbol{\rho}) = \int d^2\boldsymbol{\rho}' G_{ii}(\boldsymbol{\rho}, \boldsymbol{\rho}') m_i^n(\boldsymbol{\rho}') (i = x, z).$$

The calculated integrals for each family of modes are given in Sec. II B. The normalization integral is obtained for each kind of modes inserting in place of m_i^n the trial eigenfunctions presented in the following subsection and integrating over the dot area. In particular, for the case of mixed modes, since it is not possible to obtain an analytical expression of this integral, we have numerically evaluated it, whereas for end modes we have assumed it realistic to take the contribution from the border of the dot (see later for a discussion of this kind of modes). The other integrals are evaluated after inserting the trial eigenfunctions for m_i^n and the different contributions of the effective field for each kind of modes. At this stage the variational parameters may be chosen as the complex magnetization amplitudes m_{0i} with $i = x, z$ that are assumed proportional and in principle are left undetermined. However, it is not the aim of the present study the application of the variational approach to determine the m_{0i} for the modes different from the end modes. The minimization of the functional of Eq. (30) choosing the magnetization amplitudes as variational parameters could determine in principle the mode frequencies of each family of modes which in turn could be used to obtain the m_{0i} giving more quantitative informations about the mode profiles throughout the dot. Instead, in the following we will discuss the variational method applied only to a particular family of modes, the end modes, choosing as variational parameter the imaginary part of their complex wave vector. This choice allows us to describe the energies contributions to their frequencies and to provide realistic magnetization profiles. The quantized spectrum of the other modes is obtained directly solving the frequency functional without applying the variational method. The mode families are presented on the basis of group velocity, localization, and magnetostatic considerations using nomenclature adapted from historical work on thin films: (i) backwardlike (BA), (ii) Damon-Eshbach-like (DE), (iii) mixed (MX), and (iv) end modes.

A. Trial eigenfunctions

We present here trial solutions for Eq. (30) appropriate to each mode family giving the general expansion of a plane wave characterized by an in-plane wave vector $k = \sqrt{k_x^2 + k_y^2}$ in terms of Bessel functions of the first kind.

(i) For S modes,

$$m_i^n(\boldsymbol{\rho}) = m_0^i [\cos(k_x^n \rho \cos\phi)\cos(k_y^n \rho \sin\phi) - \sin(k_x^n \rho \cos\phi)\sin(k_y^n \rho \sin\phi)] = m_0^i \left[\left(J_0(k_n\rho) + 2\sum_{\tilde{m}=1}^{\infty} (-1)^{\tilde{m}} J_{2\tilde{m}}(k_n\rho)\cos(2\tilde{m}\phi) \right) \times \left(J_0(k_n\rho) + 2\sum_{\tilde{m}=1}^{\infty} J_{2\tilde{m}}(k_n\rho)\cos(2\tilde{m}\phi) \right) - \left(2\sum_{\tilde{m}=0}^{\infty} (-1)^{\tilde{m}} J_{2\tilde{m}+1}(k_n\rho)\cos[(2\tilde{m}+1)\phi] \right) \times \left(2\sum_{\tilde{m}=0}^{\infty} J_{2\tilde{m}+1}(k_n\rho)\sin[(2\tilde{m}+1)\phi] \right) \right]. \tag{31}$$

(ii) For AS modes,

$$m_i^n(\boldsymbol{\rho}) = m_0^i[\sin(k_x^n \rho\cos\phi)\cos(k_y^n \rho\sin\phi) + \cos(k_x^n \rho\cos\phi)\sin(k_y^n \rho\sin\phi)] = m_0^i\Bigg[\left(2\sum_{\tilde{m}=0}^{\infty}(-1)^{\tilde{m}}J_{2\tilde{m}+1}(k_n\rho)\cos[(2\tilde{m}+1)\phi]\right)$$
$$\times\left(J_0(k_n\rho) + 2\sum_{\tilde{m}=1}^{\infty}J_{2\tilde{m}}(k_n\rho)\cos(2\tilde{m}\phi)\right) + \left(J_0(k_n\rho) + 2\sum_{\tilde{m}=1}^{\infty}(-1)^{\tilde{m}}J_{2\tilde{m}}(k_n\rho)\cos(2\tilde{m}\phi)\right)$$
$$\times\left(2\sum_{\tilde{m}=0}^{\infty}J_{2\tilde{m}+1}(k_n\rho)\sin[(2\tilde{m}+1)\phi]\right)\Bigg]. \quad (32)$$

Notice the presence in the series expansions of the dependence from both the azimuthal index $\tilde{m}$ and the radial index n related to the number of nodes throughout the dot.

To generate accurate eigenfunctions we have found that it is sufficient to keep terms to order $m=2$ in Eq. (31) for S modes and $m=3$ in Eq. (32) for AS modes where m is the order of the Bessel function in the series of plane waves inside a cylinder. Indeed, due to the strongly inhomogeneous in-plane coordinate-dependent static demagnetizing field of the circular geometry, to the rotation of the static magnetization close to the dot border, and to pinning effects, even if it is possible to define a principal direction of oscillation along either x or y axis or both axes, the wave fronts of the spin modes are not planes, but they bend from the center of the dot towards the border, as also shown by calculations with a recent micromagnetic approach.[18] Therefore, differently from the vortex state[22] in mode profiles it is not possible to single out the azimuthal dependence from the radial dependence. This behavior is different from that exhibited in rectangular dots[17] where mode eigenfunctions may be approximately represented by resonant plane waves.

We have also examined truncations of the series at higher orders, $m=4$ for S and $m=5$ for AS modes, respectively, and found that the static demagnetizing integral of some of the modes slightly increases; furthermore, there is a small change in the wave-number quantization for some of the modes determined by the boundary conditions. Nevertheless, series at $m=4$ for S modes and $m=5$ for AS modes give rise to profiles that already look like plane waves that are not realistic in a saturated cylinder. A further discussion on this point showing numerical frequencies for a dot of a given radius R and thickness L obtained, taking into account higher-order Bessel series truncations and compared to that determined at $m=2$ for S and at $m=3$ for AS modes is done in the following section for the most representative modes.

Suitable trial functions are given below for each family of modes.

(i) BA modes are characterized by in-plane oscillations prevalently along the magnetization direction—i.e., along the y direction; hence, $k_x \simeq 0$. For S modes we make the following ansatz for the corresponding trial eigenfunctions:

$$m_i^n(\rho,\phi) = m_{0i}[J_0(k_n\rho) + 2J_2(k_n\rho)\cos 2\phi]. \quad (33)$$

The corresponding trial eigenfunctions for AS modes are

$$m_i^n(\rho,\phi) = m_{0i}[2J_1(k_n\rho)\sin\phi + 2J_3(k_n\rho)\sin 3\phi]. \quad (34)$$

(ii) DE modes prevalently oscillate perpendicularly to the direction of the static magnetization; hence, $k_y \simeq 0$. The trial eigenfunction for S modes are

$$m_i^n(\rho,\phi) = m_{0i}[J_0(k_n\rho) - 2J_2(k_n\rho)\cos 2\phi] \quad (35)$$

and for AS modes

$$m_i^n(\rho,\phi) = m_{0i}[2J_1(k_n\rho)\cos\phi - 2J_3(k_n\rho)\cos 3\phi]. \quad (36)$$

The eigenfunctions of Eqs. (35) and (36) may also be obtained with the transformation $\phi \rightarrow \phi + \pi/2$ applied to the trascendental functions of Eqs. (33) and (34).

(iii) MX modes do not have a preferential in-plane direction of propagation. In general, they present both BA and DE character with S and AS features. We consider in the first place MX modes with an equal number of nodes along the x and y directions; hence, it is natural to represent the corresponding eigenfunctions in the form

$$m_i^n(\rho,\phi) = m_{0i}[J_0(k_n\rho) + 2J_2(k_n\rho)\cos 2\phi][J_0(k_n\rho) - 2J_2(k_n\rho)\cos 2\phi] \quad (37)$$

for MX modes with both S BA and S DE characters and

$$m_i^n(\rho,\phi) = m_{0i}[2J_1(k_n\rho)\sin\phi + 2J_3(k_n\rho)\sin 3\phi] \times [2J_1(k_n\rho)\cos\phi - 2J_3(k_n\rho)\cos 3\phi] \quad (38)$$

for the corresponding AS ones. It is important to notice that with Eq. (37) and Eq. (38) it could be possible to represent also modes with a different number of nodes along the x- and y-directions, but we do not deal here with this case.

Moreover, modes with S BA and AS DE or S DE and AS BA mixed characters may be present and may be represented by

$$m_i^n(\rho,\phi) = m_{0i}[J_0(k_n\rho) + 2J_2(k_n\rho)\cos 2\phi][2J_1(k_n'\rho)\cos\phi - 2J_3(k_n'\rho)\cos 3\phi], \quad (39)$$

$$m_i^n(\rho,\phi) = m_{0i}[J_0(k_n\rho) - 2J_2(k_n\rho)\cos 2\phi][2J_1(k_n'\rho)\sin\phi + 2J_3(k_n'\rho)\sin 3\phi], \quad (40)$$

respectively. Here it is $k_n \neq k_n'$, because of the different number of nodes along the two in-plane directions. In the follow-

ing we will deal only with MX modes represented by the trial eigenfunctions of Eqs. (37) and (38).

(iv) End modes have recently been observed by means of the BLS technique in confined systems of different shapes. Both theoretical and micromagnetic calculations have classified these as edge modes in dots.[13,14,18] We discuss here these excitations following a different approach with respect to previous formalisms applied to stripes,[23] rectangular,[16] and circular dots[14] where the localized spin wave states have been obtained using a quantization resonance condition in a region where the internal field is strongly inhomogeneous and the corresponding end-mode wave-number is real. In particular, we describe the localization effect taking into account the behavior of these modes in the whole dot assuming trial eigenfunctions with complex wave-numbers for the corresponding dynamic magnetization components. This assumption is only a mathematical tool to describe these excitations, because the Schrödinger-like linearized equations of motion [cf. Eqs. (2) and (3)] would admit in a one-dimensional picture either a real wave vector in the lateral part of the dot (the energy of the end mode is larger than the internal field assumed equal to zero) or a purely imaginary wave vector in its central part (the energy of the internal field potential barrier is larger than the energy of the mode). In principle, in order that Eqs. (2) and (3) admit a complex wave vector a Gilbert damping term should be added to the effective field which would be responsible for the presence of an imaginary part of the frequency, yielding a negligible change of its real part. In our framework the real part of the wave vector is related with the oscillation of the mode, while the attenuation in the central part is indirectly given by the imaginary part.

The most interesting of end modes are S end modes presenting oscillations with no nodes along the direction of the static magnetization close to the dot border; as a matter of fact, among the end modes the S ones give the largest contribution to BLS intensity peaks. It is known that end modes have oscillations near the edge, but in the central part of the dot they have almost constant amplitude. We consider here also the form of the corresponding AS end modes that have a vanishing cross section. A trial eigenfunction for end modes may be based on that of BA modes assuming a complex wave-number. The dynamic magnetization components of the S modes may be represented as

$$m_i^n(\rho,\phi) = m_{0i}[J_0(k_n^{\mathrm{R}}\rho) + 2J_2(k_n^{\mathrm{R}}\rho)\cos 2\phi][J_0(\epsilon i k_n^{\mathrm{I}}\rho) + 2J_2(\epsilon i k_n^{\mathrm{I}}\rho)\cos 2\phi] \tag{41}$$

and that of the corresponding AS modes as

$$m_i^n(\rho,\phi) = m_{0i}[2J_1(k_n^{\mathrm{R}}\rho)\sin\phi + 2J_3(k_n^{\mathrm{R}}\rho)\sin 3\phi][J_0(\epsilon i k_n^{\mathrm{I}}\rho) + 2J_2(\epsilon i k_n^{\mathrm{I}}\rho)\cos 2\phi]. \tag{42}$$

A complex wave-number is defined as $k_n^{\mathrm{C}} = k_n^{\mathrm{R}} \pm i\epsilon k_n^{\mathrm{I}}$ with $\epsilon k_n^{\mathrm{I}}$ the imaginary part of the wave-number and ϵ a variational parameter. ϵ gives a measure of the localization of the spin excitations near the dot edge, and it indirectly expresses the attenuation of the oscillation in the central part of the dot. The static magnetization rotates away from the external field **H** along the y direction,[23] and end modes are partially reflected near the border. A large imaginary part of the wave-number indicates strong localization of the mode at the boundary and equivalently strong attenuation in the central part of the dot.

From previous studies we deduce that localization is related to the region of the dot where the demagnetizing field has high curvature—i.e., close to the border[23]—and its value is very close to the average value calculated along the y direction. Therefore, we consider in principle an average along the y direction rather than an average of the demagnetizing field over the whole plane. Moreover, this is appropriate for end modes we study here since they have oscillations only along the y direction. Nevertheless, the numerical value of the demagnetizing field obtained with both averages is practically the same for the dots studied here.

B. Trial eigenfunction integrals and boundary conditions

In this section we list the integrals appearing in the Ω functional after evaluation of the trial eigenfunctions given in Eqs. (33)–(38), (41), and (42). The quantized wave-number k_n is determined by the boundary conditions, and these are also given here for each set of modes. Notice that the value of k_n for each n obtained from the average over ϕ [cf. Eq. (29)] only slightly increases for a few of the S and AS MX modes and of the AS DE modes without substantially affecting their corresponding frequencies and remains unchanged for the remaining modes when trial eigenfunctions truncated at higher orders of the Bessel expansions given in Eqs. (31) and (32) (i.e., $m=4$ for S modes and $m=5$ for AS modes) are considered.

1. BA modes

We give the results of the integrals of Eq. (30) obtained after inserting the trial eigenfunctions of Eqs. (33) and (34).

(i) Normalization integral $N_{i\mathrm{S(AS)}}^{nn'} = N_{i\mathrm{S(AS)}}^{n}\delta_{nn'}$ with $N_{i\mathrm{S}}^{n} = |m_0^i|^2\pi R^2[J_0^2(k_nR) + J_1^2(k_nR) + 2J_2^2(k_nR) - 2J_1(k_nR)J_3(k_nR)]$ and $N_{\mathrm{AS}}^{n} = |m_0^i|^2 2\pi R^2[J_1^2(k_nR) + J_3^2(k_nR) - J_0(k_nR)J_2(k_nR) - J_2(k_nR)J_4(k_nR)]$.

(ii) Exchange integral $E_{i\mathrm{S(AS)}}^{n} = \alpha M_s k_n^2$.

(iii) Static demagnetizing integral. This integral is calculated numerically according to Eq. (17).

(iv) Dynamic demagnetizing integral. Since BA modes prevalently oscillate along the y direction, $k_x \simeq 0$, so that $h_x^n(\boldsymbol{\rho}) \simeq 0$. Therefore, $d_{x\mathrm{S(AS)}}^{n} \simeq 0$. Instead, from the local approximation $h_z^n(\boldsymbol{\rho}) \simeq -4\pi[1-\chi(k_nL)]m_z^n(\boldsymbol{\rho})$ and, correspondingly,

$$d_{z\mathrm{S(AS)}}^{n} = -4\pi[1-\chi(k_nL)]. \tag{43}$$

BA-mode boundary conditions are obtained inserting the eigenfunctions of Eqs. (33) and (34) into Eq. (29). In particular, we get, for S modes,

$$k_nRJ_1(k_nR) - a[J_0(k_nR) - J_2(k_nR)] = 0, \tag{44}$$

and taking $\phi' = 0$ and $\phi'' = \pi$ for AS modes (it would be equivalent considering the other half-dot) we obtain

$$\frac{2}{\pi}k_nR\left(J_0(k_nR)-\frac{2}{3}J_2(k_nR)-\frac{1}{3}J_4(k_nR)\right)+b\left[J_1(k_nR)-\frac{1}{5}J_3(k_nR)\right]=0. \quad (45)$$

The above boundary condition is valid for an odd number of nodes throughout the dot $n\geqslant 3$ including the node in the center. a and b are constants which depend on magnetic and geometric parameters. Their expressions are given in Appendix B.

2. DE modes

We insert into the integrals of Eq. (30) DE-mode trial eigenfunctions of Eqs. (35) and (36). The normalization and exchange integrals have the same expressions as for the corresponding BA modes.

(i) Static demagnetizing integral. As for BA modes this integral has been calculated numerically [cf. Eq. (17)].

(ii) Dynamic demagnetizing integral. DE modes prevalently oscillate along the x direction, so that $k_y\simeq 0$; therefore, $h_n^x(\boldsymbol{\rho})\simeq -4\pi\chi(k_nL)m_x^n(\boldsymbol{\rho})$. Hence,

$$d^n_{x\mathrm{S(AS)}}=-4\pi\chi(k_nL) \quad (46)$$

and

$$d^n_{z\mathrm{S(AS)}}=-4\pi[1-\chi(k_nL)]. \quad (47)$$

The DE-mode boundary conditions obtained solving Eq. (29) after inserting the eigenfunctions of Eqs. (35) and (36) are for S modes:

$$k_nRJ_1(k_nR)-a[J_0(k_nR)+J_2(k_nR)]=0. \quad (48)$$

For AS modes taking the half-dot limits $\phi'=\frac{\pi}{2}$ and $\phi''=\frac{3}{2}\pi$ (it would be equivalent considering the other half-dot) the calculation yields

$$\frac{2}{\pi}k_nR\left(J_0(k_nR)-\frac{2}{3}J_2(k_nR)-\frac{1}{3}J_4(k_nR)\right)+\frac{1}{2}b\left[J_1(k_nR)+\frac{7}{5}J_3(k_nR)\right]=0. \quad (49)$$

Again the above equation is valid for an odd number of nodes in the whole dot $n\geqslant 3$ including the node in the center.

3. MX modes

We insert into the integrals of Eq. (30) MX-mode trial eigenfunctions of Eqs. (37) and (38) with both S and AS BA and DE characters. Due to their less physical interest, we do not report the corresponding integrals together with the boundary conditions of MX modes presenting mixed S and AS characters whose trial eigenfunctions are expressed in Eqs. (39) and (40).

(i) Normalization integral. Since an analytical solution does not exist, we have numerically evaluated this integral.

(ii) Exchange integral $E^n_{i\mathrm{S(AS)}}=\alpha M_s\bar{k}_n^2$ where $\bar{k}_n^2=2k_n^2$.

(iii) Static demagnetizing integral. We have numerically evaluated this integral using the $N_{yy}(\rho,\phi)$ according to Eq. (17).

(iv) Dynamic demagnetizing integral. MX modes oscillate both along the x and the y directions having in our framework both k_x and k_y wave-number components. Therefore, their corresponding $h^n_{x\mathrm{S(AS)}}(\boldsymbol{\rho})\simeq -2\pi\chi(\bar{k}_nL)m_x^n(\boldsymbol{\rho})$, $d^n_{x\mathrm{S(AS)}}\simeq -2\pi\chi(\bar{k}_nL)$, and $d^n_{z\mathrm{S(AS)}}=-4\pi[1-\chi(\bar{k}_nL)]$.

Here $\bar{k}_n^2=2k_n^2$, because we deal with MX modes with equal wave-number-quantized components along the x and y directions, respectively. The corresponding boundary conditions are obtained inserting into Eq. (29) the trial eigenfunctions of Eqs. (37) and (38); for S modes, we get

$$2k_nR[J_0(k_nR)J_1(k_nR)+J_1(k_nR)J_2(k_nR)-J_2(k_nR)J_3(k_nR)]-a[J_0^2(k_nR)-2J_2^2(k_nR)]=0. \quad (50)$$

For AS modes we take for symmetry $\phi'=0$ and $\phi''=\pi/2$ (it would be equivalent to consider one of the other quarters of the dot), obtaining

$$\frac{4}{\pi}k_nR\left(J_0(k_nR)J_1(k_nR)+\frac{3}{2}J_0(k_nR)J_3(k_nR)-2J_2(k_nR)J_3(k_nR)-J_1(k_nR)J_4(k_nR)+\frac{1}{2}J_3(k_nR)J_4(k_nR)\right)+c\left(J_1^2(k_nR)+2J_1(k_nR)J_3(k_nR)-\frac{1}{3}J_3^2(k_nR)\right)=0. \quad (51)$$

As for AS BA and AS DE modes the above equation is valid for a number of nodes throughout the dot $n\geqslant 3$ both along the x and y directions considering also the node in the center. The explicit expression of the constant c depending on magnetic and geometric parameters is given in Appendix B.

A variational functional to determine the quantized spectrum for BA, DE, and MX modes may be now built up in explicit form, substituting the calculated integrals for each family into Eq. (30). The diagonal frequency spectrum assumes the following form:

$$\Omega_n^2=([H+\alpha M_s\bar{k}_n^2+D^n+4\pi M_s\chi(\bar{k}_nL)\eta]\{H+\alpha M_s\bar{k}_n^2+D^n+4\pi M_s[1-\chi(\bar{k}_nL)]\}). \quad (52)$$

$\eta=0$ for BA, $\eta=1$ for DE, and $\eta=\frac{1}{2}$ for MX modes with equal x- and y-wave-number-quantized components, respectively; in particular, $\bar{k}_n^2=k_n^2$ for BA and DE modes and $\bar{k}_n^2=2k_n^2$ for MX modes. Differently from previous approaches where it is assumed that BA modes are affected by a demagnetizing field in the center of the dot[14] and DE modes feel an average over the whole dot demagnetizing field,[13,14] we believe that the spin resonances with a number of nodes $n\neq 0$ throughout the dot are mostly affected by the strongly nonuniform demagnetizing field in the whole dot which is in general different from the averaged one and should be calculated for each mode.

It is straightforward to show that for a vanishing wave-number—i.e., $k_0=0$ in Eq. (52)—we find the Kittel equation[24] for the resonant mode in circular dots with an effective in-plane demagnetizing factor $N_\parallel$ obtained by averaging $N_{yy}(\rho,\phi)$.[13] We call this mode the fundamental (F). As

shown in recent micromagnetic calculations[18] and discussed qualitatively[14] for cylindrical dots, the energy of this mode is largely determined by the demagnetizing field at the dot center ($\rho=0$). The reason is that the mode profile is more or less uniform in the central region of the dot where the demagnetizing field is also uniform with a magnitude well approximated by the value at $\rho=0$. The lateral nonuniformity of the demagnetizing field affects the magnetization profile close to the border only, leading to strong pinning. The energy in the mode is mostly dipolar with a frequency given by

$$\Omega^2 = \{H(H + 4\pi M_s[1 - 3N_{yy}(\rho = 0)])\}. \tag{53}$$

Calculation of $N_{yy}(\rho=0)$ is accomplished via the integral of Eq. (17) for $\rho=0$:

$$N_{yy}(\rho = 0) = \frac{1}{2}R\left[\int_0^\infty dk f(kL)J_1(kR)\right] = \frac{\beta}{2(\sqrt{1+\beta^2}+1)}. \tag{54}$$

We use Eq. (53) to obtain the frequency of the F mode in the following section and note that we neglect small corrections due to both nonuniform exchange and dynamic dipolar fields related to a small, but finite wave-number.

4. End modes

We calculate the integrals of Eq. (30) inserting end-mode trial eigenfunctions of Eqs. (41) and (42).

(i) Normalization integral. Due to the localization effect close to the dot edge to simplify the calculations we evaluate this integral for $\rho=R$. We obtain $N^{nn'}_{i\mathrm{S(AS)}}(\epsilon)=N^{n}_{i\mathrm{S(AS)}}(\epsilon)\delta_{nn'}$ with

$$\begin{aligned} N^n_{i\mathrm{S}}(\epsilon) = |m^i_0|^2 2\pi R[&J_0^2(k_n^R R)J_0^2(\epsilon i k_n^I R) + 2J_2^2(k_n^R R)J_0^2(\epsilon i k_n^I R) \\ &+ 8J_0(k_n^R R)J_0(\epsilon i k_n^I R)J_2(k_n^R R)J_2(\epsilon i k_n^I R) \\ &+ 2J_0^2(k_n^R R)J_2^2(\epsilon i k_n^I R) + 6J_2^2(k_n^R R)J_2^2(\epsilon i k_n^I R)] \end{aligned} \tag{55}$$

and

$$\begin{aligned} N^n_{i\mathrm{AS}}(\epsilon) = |m^i_0|^2 4\pi R[&J_1^2(k_n^R R)J_0^2(\epsilon i k_n^I R) \\ &- 2J_1^2(k_n^R R)J_0(\epsilon i k_n^I R)J_2(\epsilon i k_n^I R) + 2J_1^2(k_n^R R)J_2^2(\epsilon i k_n^I R) \\ &+ 4J_1(k_n^R R)J_3(k_n^R R)J_0(\epsilon i k_n^I R)J_2(\epsilon i k_n^I R) \\ &- 2J_1(k_n^R R)J_3(k_n^R R)J_2^2(\epsilon i k_n^I R) + J_3^2(k_n^R R)J_0^2(\epsilon i k_n^I R) \\ &+ 2J_3^2(k_n^R R)J_2^2(\epsilon i k_n^I R)], \end{aligned} \tag{56}$$

where we assume in principle $k_n^R=k_n^I=k_n$ with k_n the quantized wave-number of nodes n of the corresponding BA mode.

(ii) Exchange integral. Because of the lateral confinement, we suppose that a good estimation of the exchange integral $E_{i\mathrm{S(AS)}}(\epsilon)=\frac{\bar{E}_{i\mathrm{S(AS)}}(\tilde{k},\epsilon)}{N_{i\mathrm{S(AS)}}(\tilde{k},\epsilon)}$ as a functional of the parameter ϵ could be obtained evaluating $\bar{E}_{i\mathrm{S(AS)}}$ for $\rho=R$ ($\tilde{k}$ is defined in the following), which may be casted in terms of Bessel functions, but since its expression is quite cumbersome, we do not report it explicitly. Since the result is independent from $i=x,z$, we put $E_{i\mathrm{S(AS)}}(\tilde{k},\epsilon)=E_{\mathrm{S(AS)}}(\tilde{k},\epsilon)$.

(iii) Static demagnetizing integral. From the considerations about end modes dynamics reported previously we evaluate $N_{yy}(\rho,\phi)$ for $\phi=\frac{\pi}{2},\frac{3}{2}\pi$, numerically averaging the result over the ρ coordinate; we indicate the result of this average with $\langle N_{yy}(\rho,\phi=\frac{\pi}{2},\frac{3}{2}\pi)\rangle_\rho$.

(iv) Dynamic demagnetizing integral. As for the case of BA modes which prevalently oscillate along the y direction $d_{x\mathrm{S(AS)}}=0$ for both S and AS modes. Instead, $h_z(\rho)\simeq -4\pi[1-\chi(\tilde{k}L)\sqrt{1+\epsilon^2}]m_z(\rho)$. The calculation of the integral leads to

$$d_{z\mathrm{S(AS)}} = -4\pi(1-\chi(\tilde{k}L)\sqrt{1+\epsilon^2}). \tag{57}$$

Therefore, the end-mode spectrum expressed in a functional form is given by

$$\begin{aligned} \Omega^2(\tilde{k},\epsilon) = \Bigg[\Bigg(H + E(\tilde{k},\epsilon) - 4\pi M_s\left\langle N_{yy}\left(\rho,\phi=\frac{\pi}{2},\frac{3}{2}\pi\right)\right\rangle_\rho\Bigg)\Bigg(H + E(\tilde{k},\epsilon) - 4\pi M_s\left\langle N_{yy}\left(\rho,\phi=\frac{\pi}{2},\frac{3}{2}\pi\right)\right\rangle_\rho \\ + 4\pi M_s[1-\chi(\tilde{k}L\sqrt{1+\epsilon^2})]\Bigg)\Bigg], \end{aligned} \tag{58}$$

where in $E(\tilde{k},\epsilon)$ the subscripts S(AS) have been omitted. The condition $\frac{\partial\Omega}{\partial\epsilon}=0$ gives the value of ϵ which minimizes the functional. The minimum of the functional of Eq. (58) is found evaluating the normalization integral $N_{\mathrm{S(AS)}}$ appearing in $E(\tilde{k},\epsilon)$ for $\epsilon=1$ corresponding to the initial assumption for which the real part of the wave-number is equal to the imaginary part and substituting in $E(\tilde{k},\epsilon)$ the appropriate $\tilde{k}$ to obtain end mode frequencies (for a discussion of this point see the following section). In this way the normalization integral is treated as a constant in the variational procedure. The ϵ found is in turn substituted into Eq. (58), taking as normalization integral that of Eqs. (55) and (56) evaluated at that ϵ.

The variational parameter ϵ is a number that gives the amount of the localization of the spin mode on the dot edge, and it also indirectly expresses its attenuation in the central

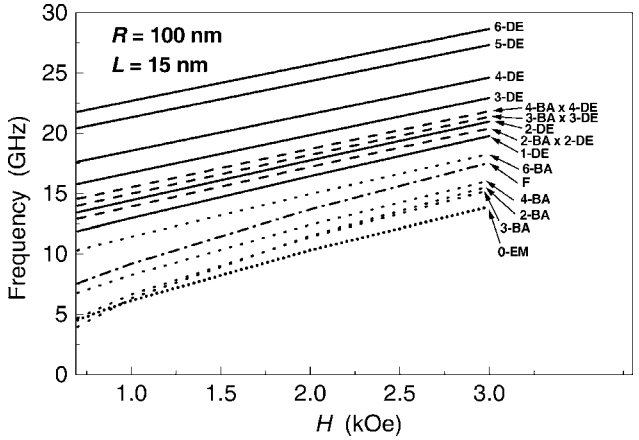

FIG. 3. Frequency dispersion of the most representative modes vs the external field H for a dot of radius $R=100$ nm and thickness $L=15$ nm. Solid lines: DE modes. Dashed lines: MX modes. Dash-dotted line: F mode. Dotted lines: BA modes. Short-dotted line: 0-EM.

part of the dot. The larger ϵ is, the more laterally localized is the mode.

III. RESULTS FOR PERMALLOY DOTS

We have applied the theory described in Sec. II to the problem of spin wave modes in saturated thin ferromagnetic cylindrical Permalloy dots with radius R ranging from the submicrometric to the micrometric scale and of thickness L on the nanometric scale. For the numerical calculations we have used the Permalloy material parameters fitted to the BLS data reported in Ref. 14 of the continuous film: $4\pi M_s = 9.5$ kOe, $\gamma/2\pi = 2.996$ GHz/kOe, and $\alpha/4\pi = 2.42 \times 10^{-13}$ cm^2.

First, we have determined the spin wave frequencies as a function of the applied field H for fixed R and L. We present the calculations for a dot of radius $R=100$ nm and thickness $L=15$ nm at an external field H ranging from 0.7 kOe to 3 kOe. As a matter of fact, it is known from micromagnetic calculations[18] that for a dot of this size there is a first-order transition from the vortex to the saturated-state at about $H=0.7$ kOe. We are concerned here only with this high-field-saturated state.

The results of frequency calculations for representative modes of S and AS nature in a Permalloy sample are shown in Fig. 3. Modes are numbered by the following scheme. The lowest order DE mode is 1-DE, for example, and the nth-order mode of family F is n-F. The order n corresponds to the quantization number n that gives the number of nodes throughout the dot. The frequency dispersion versus H is mainly a linear function of the external field except for the low-field behavior of the low-frequency BA modes (2-BA and 3-BA). An exception is represented by the F-mode frequency that increases rapidly with increasing H with a slope greater than that of the other modes. DE frequencies increase with increasing n, while BA ones can increase or decrease due to the competition between exchange and the dipolar interactions.[14,18,23] For this case the minimum frequency of BA branch belongs to the 3-BA mode at high field ($H > 2$ kOe) and to the 2-BA one for $H < 2$ kOe due to a crossing between the two frequencies at H about 2 kOe.

TABLE I. Calculated frequencies of the most representatives modes determined with the present analytical model compared to that obtained with the micromagnetic calculations taken from Ref. 18. The units are in GHz.

	$H=2.7$ kOe		$H=2.9$ kOe	
	4-BA	2-DE	4-BA	2-DE
Analytical	15.00	20.01	15.72	20.64
Micromagnetic	15.15	19.62	15.82	20.23
BLS	15.40	19.70	16.40	20.40

The static demagnetizing integral D^n is different for each spin excitation. In particular, for BA modes it has an oscillatory behavior at low n, reaches a maximum for $n=6$, and then it does not vary appreciably, whereas for DE modes the integral decreases with increasing n and becomes almost constant for $n>6$. Numerical values of D^n found for BA and DE spin modes represented in Fig. 3 are $D^2=0.060$, $D^3=0.072$, $D^4=0.067$, and $D^6=0.070$ for BA modes and $D^1=0.081$, $D^2=0.070$, $D^3=0.065$, $D^4=0.062$, $D^5=0.060$, and $D^6=0.059$ for DE modes.

The averaged effective demagnetizing factor over the dot plane, $N_{\|}$, calculated in recent studies for the determination of the frequency spectrum in tangentially magnetized cylindrical dots[13,14] represents only an approximation to the exact results. For the dot considered here the averaged value is $N_{\|}=0.083$ and is in general different from our calculated D^n for each n. More accurate estimates of D^n, such as those given here, are therefore important for accurate estimates of individual mode frequencies.

Also in Fig. 3 MX mode frequencies for modes with an equal number of nodes along the x and y directions are shown. It is interesting to note that MX-mode frequencies are in general lower than the corresponding DE ones with the same wave-number. Oscillations in these modes reduce the x component of the dipolar field by roughly one-half that of DE modes for each k_n. The corresponding static D^n depends again on the mode index n; in particular, for the first modes it is $D^2=0.064$, $D^3=0.043$, and $D^4=0.054$.

Finally, in Fig. 3 we have shown the frequencies of the 0-EM (end mode) which has lateral oscillations in the dot. This mode has the lowest frequency of all in several geometries[14,23] and is already classified as EM in Ref. 18. This mode and its family will be discussed in more detail later in the paper.

In Table I a comparison of representative mode frequencies for $R=100$ nm and $L=15$ nm is shown as calculated by our analytical model and ones obtained using a micromagnetic approach based on a dynamical matrix formalism.[18] Results are given for two different values of the applied field H. Experimentally measured BLS frequencies of each mode have been given for comparison.[18,25]

The agreement between the analytical and the micromagnetic calculated frequencies is excellent for the 4-BA mode with a numerical difference of about 1% for both applied

TABLE II. Frequencies of the F mode for $R=100$ nm at three different thicknesses. BLS data and micromagnetic frequencies are taken from Ref. 18 for $L=15$ nm. For $L=24$ nm the available BLS data are taken from Ref. 25 and for $L=50$ nm from Ref. 14. The units are in GHz.

	$L=15$ nm			$L=24$ nm		$L=50$ nm	
	1.1 kOe	1.9 kOe	2.7 kOe	1 kOe	3 kOe	1 kOe	3 kOe
Analytical	9.70	13.28	16.43	8.89	17.06	8	15.69
Micromagnetic	9.62	13.14	16.20				
BLS	9.90	13.40	16.30	8.40	16.68	8	15.36

fields. It is important to notice that the 4–BA mode could also be classified as a 2–BA mode, because of the presence of two nodal planes close to the boundary that may be related to the pinning effect and not considered as real nodes. However, in order to adopt the same assignment as for the case of the cylindrical dots studied with a micromagnetic approach we have preferred in this work to include in the classification also the nodes close to the dot border. The comparison is still very good also for the 2-DE mode although the analytically calculated frequency is larger than the micromagnetic one by about 2%. The reason for these discrepancies may be related to the assumption that the static magnetization is uniformly distributed along the y axis in the analytical calculations, while in the micromagnetic approach the effect of the nonuniformity of $\mathbf{M}_0$ close to the dot lateral surface is taken into account. Another source of differences with respect to the micromagnetic calculated frequencies could be due to the local approximation used for the calculation of the dynamic dipolar field within the present model. Finally, another reason of slight discrepancy may be due to the value of the saturation magnetization that in the micromagnetic calculations is larger than about 6% with respect to the one of the present model; nevertheless, this effect is almost totally counterbalanced by a value of the gyromagnetic ratio in the micromagnetic approach smaller than about 2%. The agreement of the analytical frequencies with the BLS ones is very good with a difference of about 2% for the 2–DE mode and at most about 4% for the 4–BA mode.

Finally, we have calculated the frequencies of both the 4-BA and the 2-DE modes for the same geometry truncating the Bessel series expansion of Eq. (31) at a higher order—i.e., for $m=4$. We have found that the corresponding frequencies are shifted down at most of about 0.3 GHz for the whole range of applied field studied, because of a slight change of the demagnetizing integral of some of the modes studied. For example, at $H=2.7$ kOe the 2-DE mode demagnetizing integral D^2 increases from 0.070 to 0.081 and the frequency results 19.68 GHz, while the 4-BA mode demagnetizing integral D^4 increases from 0.067 to 0.077, yielding a frequency of 14.66 GHz. Even if the agreement with the micromagnetic calculations improves at least for the 2-DE mode frequency, the resulting profiles of the modes already look like plane waves losing their radial character; hence, we believe that a truncation of the Bessel series for S modes at a order higher than $m=2$ is not realistic. Also for some of the S MX modes the truncation of the corresponding series at a higher order yields an increase of their demagnetizing integral and a small change of the wave-number, resulting in a change of the frequency. In particular, the frequency of the 2-BA $\times$ 2-DE decreases more than 1 GHz, whereas for the 4-BA $\times$ 4-DE modes the frequency increases the same amount for the whole range of applied fields. Nevertheless, also for these modes the corresponding profiles have already the form of plane waves oscillating both along x and y directions and are not anymore the proper eigenfunctions in a saturated cylinder. The same conclusions may be drawn examining truncation of the expansion at $m=5$ of Eq. (32) for the 3-BA $\times$ 3-DE MX modes. Therefore, we think that also for these modes the truncation at the lower order is more realistic.

In order to test further the resonance formula for the F mode given by Eq. (53), in Table II a comparison between frequencies calculated at different applied fields H and those obtained by BLS experiment is provided. The experiments were performed on Permalloy dots with $R=100$ nm at $L=15$ nm,[18] $L=24$ nm,[25] and $L=50$ nm.[14] For $L=15$ nm we also list frequencies determined by the micromagnetic technique[18] for reference although values for the two largest L dots are not available. The frequencies determined according to Eq. (53) compare very well with the BLS data for dots of $L=15$ nm and $L=50$ nm and also with the micromagnetic frequencies. The agreement between experiment and our theory is less good for $L=24$ nm even if the numerical discrepancy is at most of about 6%.

In Fig. 4 the spatial distribution of the dynamic magnetization component $m_x(\rho,\phi)$ is profiled for some of the spin modes. The profiles are presented as amplitudes across the dot for the case $R=100$ nm and $L=15$ nm. In panel (a) the F-mode eigenfunction is seen to have a maximum in the center and has no nodes. This mode is strongly pinned along the border in the y direction. The evaluation of the pinning parameter along the y axis gives $p(\phi=\frac{\pi}{2},\frac{3}{2}\pi)=81$ and describes strong pinning along the $\mathbf{M}_0$ direction. p has smaller values for other azimuthal angles corresponding to smaller pinning. Note that the dynamic pinning parameter p_d mostly gives only a small correction relative to the static one p_s. Similar pinning properties are found for the other spin wave modes since p is independent from the mode index n, even though the magnitude of the pinning is in general different for each mode.

Note that in our theory the F mode is purely magnetostatic and corresponds to a vanishing wave-number. This behavior is different from that found for the F mode in the vortex state[14] where its corresponding wave-number is calculated as the first nonvanishing solution of the radial boundary conditions. In the vortex configuration the F-mode frequency is mainly affected by both the nonuniform exchange and the volume dynamic dipolar fields.

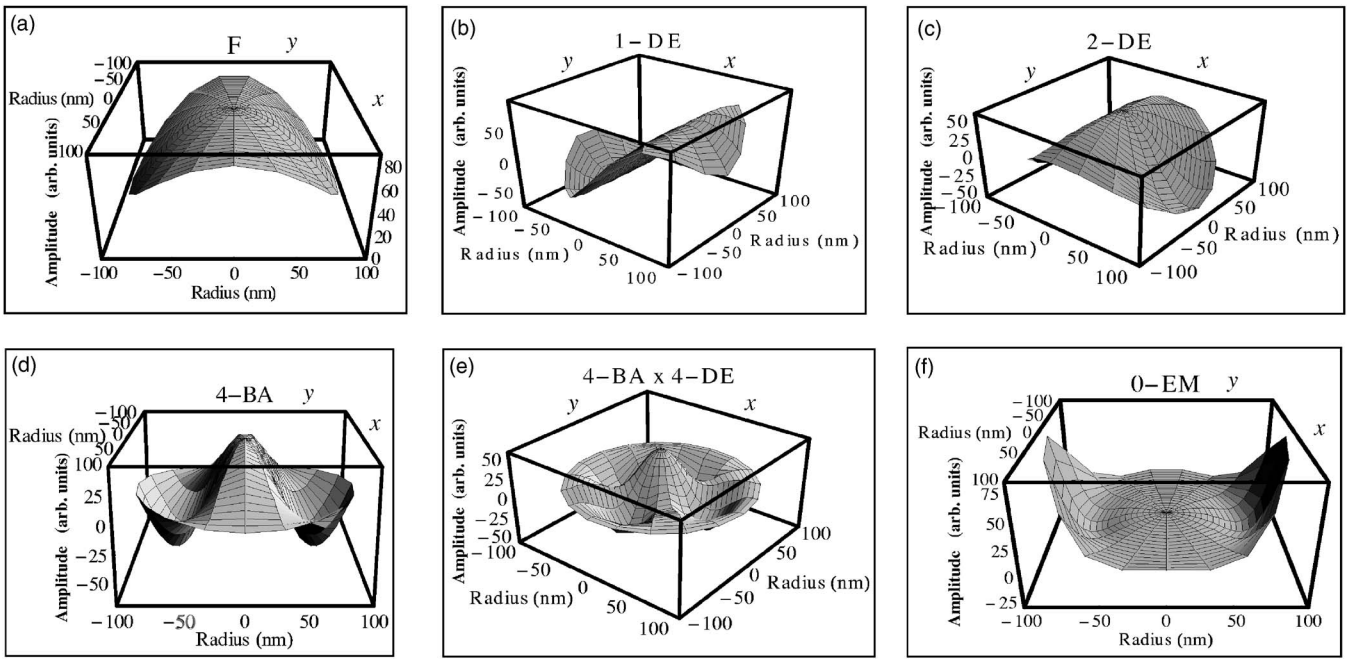

FIG. 4. Spatial profiles of the calculated $m_x^n(\rho,\phi)$ eigenfunction for $R=100$ nm and $L=15$ nm of some of the spin modes. Panel (a): F mode. Panel (b): 1-DE. Panel (c): 2-DE. Panel (d): 4-BA. Panel (e): 4-BA$\times$4DE. Panel (f): 0-EM. The meaning of the symbols labeling the modes is the same as in Fig. 3.

Profiles of two typical DE spin modes of the spectrum, 1-DE and 2-DE, are shown in panels (b) and (c). The first one is antisymmetric with respect to a plane perpendicular to the dot surface containing the y axis (its nodal plane). Since for this mode the AS DE boundary conditions of Eq. (49) are not applicable (it is valid only for AS modes with nodes $n \geqslant 3$), we suppose that, in analogy to the F mode, this excitation is strongly pinned at the boundary in the region close to the x axis. The obtained wave-number here is $k_1=3.05\times10^5$ cm^{-1}. The 2-DE mode is symmetric with respect to a plane containing **H** and has two nodal surfaces parallel to the y axis. The corresponding wave-number obtained from the boundary condition of Eq. (48) is $k_2=3.83\times10^5$ cm^{-1}. This mode is unpinned in the region close to the x direction but becomes more pinned along the other directions.

The 4-BA mode of panel (d) is symmetric with respect to a plane perpendicular to the dot surface containing the x axis and has four nodal surfaces parallel to the x direction. This mode is strongly pinned at the border close to the y direction and rather unpinned along the other directions. The 4-BA wave-number, the second solution of the boundary conditions of Eq. (44), is $k_4=5.26\times10^5$ cm^{-1}. We have found that this solution is also well approximated by applying the radial boundary condition (along the y axis) under the hypothesis of strong pinning. The wave-number in this case is $k_4=5.27\times10^5$ cm^{-1}.

In panel (e) a MX-mode profile is indicated as 4-BA $\times$4-DE. This mode is symmetric with respect to any plane perpendicular to the dot surface with a maximum amplitude in the dot center. The mode has four nodal surfaces parallel to both **H** and to the x axis and mixes features of BA and DE modes. The corresponding wave-number has equal x and y components and calculated from Eq. (50) is $k_4=5.2\times10^5$ cm^{-1}. This mode is strongly pinned in each in-plane direction.

Finally, we discuss the 0-EM profile as representative of end modes. The example shown in panel (f) of Fig. 4 was obtained by finding the value of the variational parameter ϵ, making the functional Ω of Eq. (58) a minimum. The mode profile has a small oscillation along the y axis of the dot with no nodal surfaces parallel to the x axis. It is symmetrically localized near the edges, while in the central part of the dot the amplitude is essentially uniform.

The first interval with real k_n^R of the complex wave-number for which the functional of Eq. (58) has a minimum that determines that an end mode is between k_4^R and k_6^R, corresponding to the second and third solutions of the boundary conditions for S BA modes as determined by Eq. (44). We assign the corresponding real part of the wave-number for the 0-EM mode the mean of k_4^R and k_6^R of the considered interval. This assignment has the value $\tilde{k}=6.9\times10^5$ cm^{-1} for our example. The ϵ value obtained at high applied field ($H=3$ kOe) is $\epsilon=0.80$, and neglecting its slight dependence from H we take it for over the entire range of applied fields studied. Moreover, increasing the external field increases the height of the potential barrier in the central part of the dot, creating multiple localized states,[26] even if as stated it does not substantially affect the edge localization of the single mode.

The other end modes have a complex structure with oscillations in the direction perpendicular to the applied field **H**. These modes have features of EM- and DE-mode families that could be in principle an analogy to MX modes. We do not discuss these here but note that their structure is in general complex.

Additional solutions of the boundary condition of Eq. (44) which minimize the functional Ω of Eq. (58) in the next

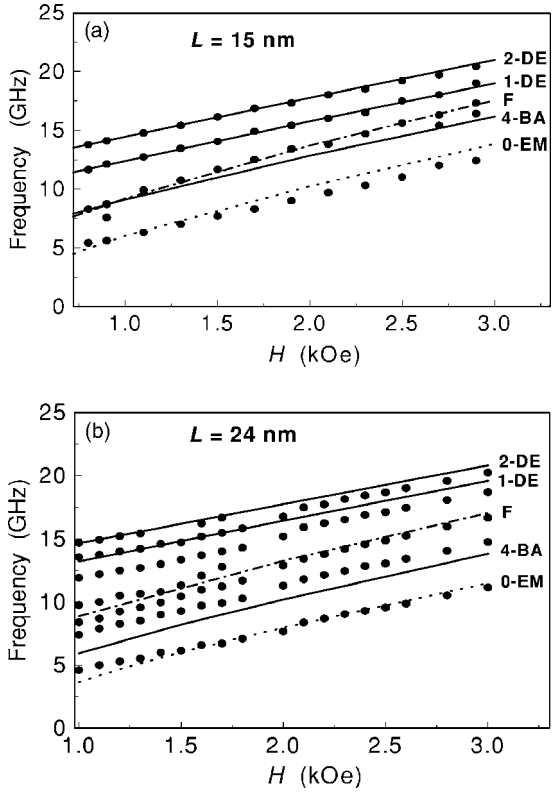

FIG. 5. Panel (a): frequency vs H for $R=100$ nm and $L=15$ nm of the most representative spin modes. Solid lines: calculated DE and BA frequencies. Dash-dotted line: calculated F mode frequency. Dotted line: calculated 0-EM frequency. Circles: BLS frequencies. Panel (b): frequency vs H for $R=100$ nm and $L=24$ nm of the most representative spin modes. The meaning of the lines and of the symbols is the same as in panel (a).

interval of k_n correspond to the second S EM. This solution has no nodal surfaces but does display a different localization to the dot border.

From the boundary condition of Eq. (45) for AS BA modes and from Eq. (58) it is possible to obtain the eigenfrequency and eigenfunction profiles of the corresponding AS 0-EM. We have found that the wave-number which satisfies the condition of Eq. (58) is $\tilde{k}=5.4\times10^5$ cm^{-1}, corresponding to $\epsilon=0.70$, again obtained for $H=3$ kOe. The resulting frequency dispersion versus H is almost degenerate with respect to that of the 0-EM. These results agree with that of micromagnetic calculations[18] where a pair of almost degenerate modes, one symmetric and the other antisymmetric with respect to a plane perpendicular to the applied field, were found.

A comparison to experimental data from Permalloy dots obtained using BLS (Refs. 18 and 25) is given in Fig. 5. Note that the BLS measurements have been carried out in arrays of dots with a separation between adjacent dots equal to the dot diameter $2R$; therefore, the interdot coupling may be considered negligible in the experiment. The comparison is performed for $L=15$ nm [panel (a)] and $L=24$ nm [panel (b)]. The theoretical frequencies, calculated using our variational theory with Permalloy parameters given earlier, are in good agreement with the $L=15$ nm data. The good fit between experiment and theory allows us to identify unambiguously the different mode families and node number. The 0-EM demagnetizing factor, evaluated along the y direction and averaged over ρ, is $\langle N_{yy}(\rho,\phi=\frac{\pi}{2},\frac{3\pi}{2})\rangle_\rho=0.083$. This value is larger than those associated with the other modes and is the reason the 0-EM mode has the lowest frequency in the spectrum.

In general, S modes give the largest contribution to the scattering cross section, but due to the phase-displacement of light along the direction of oscillation of the mode the AS modes with a low number of nodes may contribute also even if their scattering cross section is small. This is the case for the 1-DE mode depicted in Fig. 5 which has a node in the center of the dot and is antisymmetric with respect to the plane containing H perpendicular to the dot surface.

The agreement between the 0-EM calculated frequency and the measured one is satisfactory at $L=15$ nm where the experimental frequency is overestimated at high fields and improves at $L=24$ nm, especially at high fields. This high-field discrepancy could be related to a possible overestimation of the dynamic exchange field which is supposed to affect the end-mode dynamics from its contributions from the border. Moreover, the exchange field is very sensitive to slight changes of the variational parameter ϵ. Note also that the low-field 0-EM frequency, especially at $L=24$ nm, is underestimated by our theory. End modes can be sensitive to magnetization inhomogeneities close to the border for small applied fields especially in the range of H where the phase transition from the saturated to the vortex state takes place. The variational parameter ϵ does not fully reproduce the effect of such inhomogeneities and also fails to take into account possible contributions from the dynamic exchange fields introduced by border inhomogeneity at low H.

The agreement between calculated and measured frequencies is less convincing for the $L=24$ nm dots shown in panel (b), particularly for the 4-BA mode. As mentioned earlier, it is possible that our neglect of the z dependence for the dynamic magnetization is significant for thicknesses $L>20$ nm. We expect that the introduction of a nonuniform magnetization along the thickness of the dot would upshift the 4-BA frequency towards the experimental value in the range of applied field considered, because of an increasing of the dynamic exchange energy related to the quantization of the k wave vector along the thickness. A simple model recently introduced to describe BA spin modes in moderate aspect ratios dots ($\beta=0.5$) in terms of stationary waves and analogous to the magnetic film volume backward modes[14] support this interpretation.

The 2-DE theoretical frequencies compare reasonably well with the experimental ones; a significant discrepancy exists for the 1-DE modes, where the experimental frequency seems to be overestimated especially at high fields. In addition to the possible failure of the thin-film approximation, it is worth noting that these modes also have a large experimental uncertainty in frequency due to the ambiguity of a rather broad scattering cross section. For the present case the uncertainty for both modes is about ± 0.2 GHz. Furthermore, at low applied fields ($H<2$ kOe) there are two additional experimental modes between the calculated F and 1-DE that do not find a counterpart in the theory and that are not

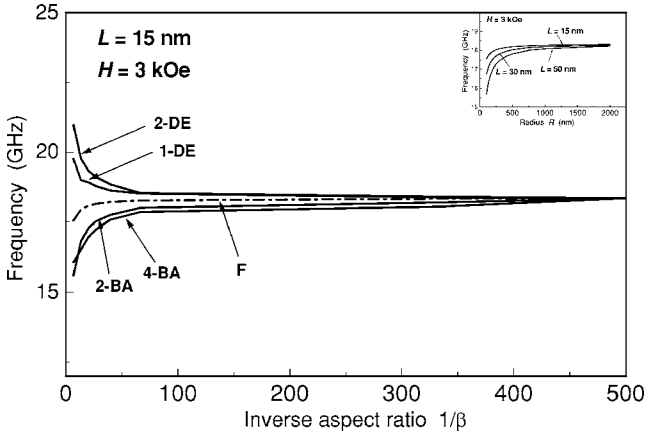

FIG. 6. Frequencies vs inverse aspect ratio $1/\beta$ at a fixed thickness $L=15$ nm of some of the most representative modes for an applied field $H=3$ kOe. Solid lines: DE and BA modes. Dash-dotted line: F mode. Inset: F-mode dispersion vs R for three different thicknesses at $H=3$ kOe.

present at high fields. They could be residual vortex-state modes present in a region of applied fields close to the vortex to the saturated-state phase transition occurring at $H \simeq 1$ kOe for this aspect ratio. Finally, the quality of the spectra at $L=24$ nm is not so good as at $L=15$ nm.

The 0-EM mode has $\epsilon=0.82$ in our theory and a ρ-averaged demagnetizing tensor component $\langle N_{yy}(\rho, \phi = \frac{\pi}{2}, \frac{3\pi}{2})\rangle_\rho = 0.115$. These give a frequency at fixed H that is downshifted with respect to the $L=15$ nm case.

We present our last calculation in this paper in Fig. 6 where we show the dependence of the spin wave frequencies on the inverse aspect ratio $1/\beta$. Our calculations are for $H=3$ kOe and for $L=15$ nm thick dots. Mode frequencies for small $1/\beta$ merge asymptotically as the inverse aspect ratio tends to infinity. For $1/\beta > 400$ they approach the frequency resonance limit of the corresponding continuous film, $\Omega = [H(H+4\pi M_s)]^{1/2}$. BA-mode dispersions increase monotonically with increasing $1/\beta$, while the DE-mode frequencies decrease.

The nonuniform exchange field and the static demagnetizing field tend to zero with increasing $1/\beta$ for each mode. Also, the z component of the dynamic dipolar field h_d^z increases in modulus with increasing $1/\beta$ towards the value $4\pi M_s$ for each mode. The h_d^x component of BA modes is already vanishingly small at low $1/\beta$, resulting in an overall increase in BA-mode frequencies. By way of contrast, the smaller value of the static demagnetizing field with increasing $1/\beta$ is responsible for the suppressed frequency of the F mode.

DE-mode frequencies decrease at large $1/\beta$ because the h_d^x component decreases in modulus with increasing $1/\beta$ whereas h_d^z grows in modulus with it, leading to an overall decrease in the frequencies.

The frequency of the F mode is shown as a function of dot radius for three different thicknesses in the inset to Fig. 6. The field is $H=3$ kOe. There is a monotonic increase in the frequencies with R, and the mode frequencies approach the resonant frequency limit of the continuous film as R becomes infinite.

Finally, we note that the frequency of the F mode at fixed radius R decreases as L is increased. This behavior is opposite to that found for the F mode in the vortex state at zero applied field for the same range of thicknesses.[22]

IV. SUMMARY

A theory of spin wave modes confined in a tangentially magnetized cylinder has been formulated using a variational approach. Results for mode frequencies and profiles have been obtained for Permalloy dots. A comparison to data taken from BLS experiments on Permalloy dots has been made.

Useful trial eigenfunctions able to accurately reproduce the most important resonances have been proposed and their validity explored through comparison to micromagnetic results for small dots in addition to comparison with experiment. A quantization condition derived from the magnetic film Rado-Weertman boundary condition taking into account the in-plane coordinate dependence of the dynamic magnetization has been obtained for each family of modes. Expressions are given for the calculation of characteristic parameters governing mode pinning and for effective wavenumbers describing mode propagation. Our theory is particularly useful for the calculation of modes in dots of small aspect ratio and large radius.

The main approximation remaining in the theory is the thin-film assumption in which the dynamic magnetization is supposed to be uniform across the film thickness. Removal of this constraint and the inclusion of interdot dipolar coupling in arrays of interacting dots would result in a useful extension of the model. Finally, it would be interesting to generalize the present formalism to tangentially magnetized elliptical dots, taking into account the effect of the eccentricity and of the orientation of the applied field on the spin dynamics.

ACKNOWLEDGMENTS

Work at the Italian Institution was supported by CNR-INFM, Project No. FIRB-RBNE017XSW. The authors acknowledge G. Gubbiotti and G. Carlotti for permission to reproduce unpublished Brillouin Light Scattering data. R.L.S. also acknowledges support from the Australian Research Council.

APPENDIX A: DEMAGNETIZING TENSOR COMPONENTS

In this Appendix the calculation of the static demagnetizing factor tensor components N_{xy} and N_{yy} is presented. In particular,

$$N_{xy}(\rho, \phi) = \frac{1}{2} I_a \sin 2\phi \tag{A1}$$

and

$$N_{yy}(\rho, \phi) = I_a \sin^2 \phi + I_b \cos 2\phi, \tag{A2}$$

where, omitting the ρ dependence, $I_a = R\int_0^\infty dk \chi(kL) J_1(kR) J_0(k\rho)$ and $I_b = R\int_0^\infty dk \chi(kL) J_1(kR) \frac{J_1(k\rho)}{k\rho}$.

Substituting $\chi(kL)=1-\frac{1-e^{-kL}}{kL}$ it is $I_a=I_1+I_2+I_3$ and $I_b=I_4+I_5+I_6$. In particular,

$$I_1 = R\int_0^\infty dk J_1(kR)J_0(k\rho) = \begin{cases} 1 & \text{if } \rho < R, \\ 1/2 & \text{if } \rho = R, \end{cases} \tag{A3}$$

$$I_2 = -\frac{1}{\beta}\int_0^\infty dk \frac{J_1(kR)J_0(k\rho)}{k} = -\frac{2}{\pi\beta}E\left[\frac{\rho^2}{R^2}\right], \tag{A4}$$

where E is the complete elliptic integral:

$$I_3 = \frac{1}{\beta}\int_0^\infty dk \frac{J_1(kR)J_0(k\rho)}{k}e^{-kL}. \tag{A5}$$

Using the Gegenbauer addition theorem on the Bessel functions I_3 may be expressed as

$$I_3 = \left[\frac{R\Gamma[1]}{2\beta\Gamma\left[\frac{3}{2}\right]\Gamma\left[\frac{1}{2}\right]}\right] \times \int_0^\pi d\tilde{\varphi}\frac{\sin^2\tilde{\varphi}}{(L^2+2iLR\cos\tilde{\varphi}-R^2\cos^2\tilde{\varphi}+\rho^2)^{1/2}}, \tag{A6}$$

where $\Gamma[x]$ is the Euler function; in particular, $\Gamma[1]=1$, $\Gamma\left[\frac{3}{2}\right]=\frac{\sqrt{\pi}}{2}$, and $\Gamma\left[\frac{1}{2}\right]=\sqrt{\pi}$. The integral may be solved analytically and is expressed in terms of elliptic integrals of the first kind $F[\varphi,k]$, elliptic integrals of the second kind $E[\phi,\bar{k}]$ and $E\left[\frac{1}{\varphi},\frac{1}{\bar{k}}\right]$, and incomplete elliptic integrals of the third kind $\Pi[\bar{n},\phi,\bar{k}]$. φ, k, $\bar{k}$, ϕ, $\frac{1}{\varphi}$, $\frac{1}{\bar{k}}$, and $\bar{n}$ are different arguments of the complete elliptic integrals.

The integral I_4 is

$$I_4 = R\int_0^\infty dk J_1(kR)\frac{J_1(k\rho)}{k\rho} = \frac{1}{2}. \tag{A7}$$

I_5 is instead

$$I_5 = \frac{1}{\beta}\int_0^\infty dk J_1(kR)\frac{J_1(k\rho)}{k^2\rho} = \frac{1}{2\beta}{}_2F_1\left[-\frac{1}{2},\frac{1}{2},2,\frac{\rho^2}{R^2}\right], \tag{A8}$$

with ${}_2F_1\left[-\frac{1}{2},\frac{1}{2},2,\frac{\rho^2}{R^2}\right]$ the hypergeometric function, and finally

$$I_6 = \frac{1}{\beta}\int_0^\infty dk J_1(kR)\frac{J_1(k\rho)}{k^2\rho}e^{-kL}. \tag{A9}$$

Using again the Gegenbauer addition theorem we get

$$I_6 = \frac{\Gamma[1]}{\pi\beta^2\Gamma[3]}\int_0^\pi d\tilde{\varphi}\,{}_2F_1\left[\frac{1}{2},1,2,-\frac{\rho^2+R^2-2\rho R\cos\tilde{\varphi}}{L^2}\right]\sin^2\tilde{\varphi}, \tag{A10}$$

where $\Gamma[3]=2$. The solved integral is a combination of elliptic integrals of the first kind $F[\varphi,k]$, complete elliptic integrals of the first kind $K[\varphi,\hat{k}]$, elliptic integrals of the second kind $E[\phi,\bar{k}]$ and $E\left[\frac{1}{\varphi},\frac{1}{\bar{k}}\right]$, and incomplete elliptic integrals of the third kind $\Pi[\bar{n},\phi,\bar{k}]$. Again φ, k, $\bar{k}$, $\hat{k}$, ϕ, $\frac{1}{\varphi}$, $\frac{1}{\bar{k}}$, and $\bar{n}$ are different arguments of the complete elliptic integrals.

APPENDIX B: BOUNDARY CONDITIONS

To determine the static pinning parameter p_s of Eq. (27) we need $N_{yy}(R,\phi,\beta)$. The calculation of the integrals of Eq. (17) in the limit for $\rho\to R$ gives

$$N_{yy}(R,\phi,\beta) = \left(\frac{1}{2}-\frac{2}{\pi}\frac{1}{\beta}+\frac{1}{\pi}E\left[-\frac{4}{\beta^2}\right]\right)\sin^2\phi + \left(\frac{1}{2}{}_2F_1\left[-\frac{1}{2},\frac{1}{2},2,-\frac{4}{\beta^2}\right]-\frac{4}{3\pi}\frac{1}{\beta}\right)\cos 2\phi. \tag{B1}$$

In order to evaluate the dynamic part of the pinning parameter p_d given in Eq. (28) the calculation of the integral $I_{p_d}(\beta)$ is required. We use the Fourier decomposition given in Eq. (13), we integrate z and z' along the dot thickness and then over k, getting

$$I_{p_d}(\beta) = \frac{1}{2}{}_2F_1\left[-\frac{1}{2},\frac{1}{2},2,-\frac{4}{\beta^2}\right]-\frac{4}{3\pi}\frac{1}{\beta}. \tag{B2}$$

Also the constants a, b, and c, of the boundary conditions of Eqs. (44) and (45), Eqs. (48) and (49), and Eqs. (50) and (51) are reported in this Appendix:

$$a = \tau\left(\frac{\pi}{4}+\frac{1}{3}\frac{1}{\beta}+\frac{1}{2}E\left[-\frac{4}{\beta^2}\right]-\frac{\pi}{2}{}_2F_1\left[-\frac{1}{2},\frac{1}{2},2,-\frac{4}{\beta^2}\right]\right), \tag{B3}$$

$$b = \tau\left(\frac{4}{3}+\frac{16}{9}\frac{1}{\pi}\frac{1}{\beta}+\frac{8}{3}\frac{1}{\pi}E\left[-\frac{4}{\beta^2}\right]-\frac{8}{3}{}_2F_1\left[-\frac{1}{2},\frac{1}{2},2,-\frac{4}{\beta^2}\right]\right), \tag{B4}$$

$$c = \tau\left(1+\frac{4}{3}\frac{1}{\pi}\frac{1}{\beta}+2\frac{1}{\pi}E\left[-\frac{4}{\beta^2}\right]-2{}_2F_1\left[-\frac{1}{2},\frac{1}{2},2,-\frac{4}{\beta^2}\right]\right), \tag{B5}$$

with $\tau=\frac{1}{2\pi}\frac{R^2}{l_0^2}$.

[1] C. Mathieu, J. Jorzick, A. Frank, S. O. Demokritov, A. N. Slavin, B. Hillebrands, B. Bartenlian, C. Chappert, D. Decanini, F. Rousseaux, and E. Cambril, Phys. Rev. Lett. **81**, 3968 (1998); J. Jorzick, S. O. Demokritov, C. Mathieu, B. Hillebrands, B. Bartenlian, C. Chappert, F. Rousseaux, and A. N. Slavin, Phys. Rev. B **60**, 15194 (1999).

[2] J. Jorzick, S. O. Demokritov, B. Hillebrands, B. Bartenlian, C. Chappert, D. Decanini, F. Rousseaux, and E. Cambril, Appl. Phys. Lett. **75**, 3859 (1999); J. Appl. Phys. **87**, 5082 (2000).

[3] S. Demokritov and B. Hillebrands, in *Spin Dynamics in Confined Magnetic Structures I*, Springer Series in Topics in Applied Physics, edited by B. Hillebrands and K. Ounadjela (Springer-Verlag, Berlin, 2002), p.65.

[4] K. Yu. Guslienko, S. O. Demokritov, B. Hillebrands, and A. N. Slavin, Phys. Rev. B **66**, 132402 (2002).

[5] Y. Roussigné, S. M. Chérif, C. Dugautier, and P. Moch, Phys. Rev. B **63**, 134429 (2001).

[6] P. C. Fletcher and C. Kittel, Phys. Rev. **120**, 2004 (1960).

[7] K. Abe and I. Ikushima, J. Appl. Phys. **42**, 361 (1971).

[8] R. Arias and D. L. Mills, Phys. Rev. B **63**, 134439 (2001).

[9] R. Arias and D. L. Mills, Phys. Rev. B **67**, 094423 (2003).

[10] R. Arias and D. L. Mills, Phys. Rev. B **70**, 094414 (2004).

[11] G. N. Kazakei, P. E. Wigen, K. Yu. Guslienko, V. Novosad, A. N. Slavin, V. O. Golub, N. A. Lesnik, and Y. Otani, Appl. Phys. Lett. **85**, 443 (2004).

[12] G. N. Kakazei, P. E. Wigen, K. Yu. Guslienko, R. W. Chantrell, N. A. Lesnik, V. Metlushko, H. Shima, K. Fukamichi, Y. Otani, and V. Novosad, J. Appl. Phys. **93**, 8418 (2003).

[13] K. Yu. Guslienko and A. N. Slavin, J. Appl. Phys. **87**, 6337 (2000).

[14] G. Gubbiotti, G. Carlotti, T. Okuno, T. Shinjo, F. Nizzoli, and R. Zivieri, Phys. Rev. B **68**, 184409 (2003).

[15] R. I. Joseph and E. Schlömann, J. Appl. Phys. **36**, 1579 (1965).

[16] K. Y. Guslienko, R. W. Chantrell, and A. N. Slavin, Phys. Rev. B **68**, 024422 (2003).

[17] M. Grimsditch, L. Giovannini, F. Montoncello, F. Nizzoli, Gary K. Leaf, and Hans G. Kaper, Phys. Rev. B **70**, 054409 (2004).

[18] L. Giovannini, F. Montoncello, F. Nizzoli, G. Gubbiotti, G. Carlotti, T. Okuno, T. Shinjo, and M. Grimsditch, Phys. Rev. B **70**, 172404 (2004).

[19] G. T. Rado and J. R. Weertman, J. Phys. Chem. Solids **11**, 315 (1959).

[20] George T. Rado, Phys. Rev. B **26**, 295 (1982).

[21] L. R. Walker, Phys. Rev. **105**, 390 (1957).

[22] R. Zivieri and F. Nizzoli, Phys. Rev. B **71**, 014411 (2005).

[23] J. Jorzick, S. O. Demokritov, B. Hillebrands, M. Bailleul, C. Fermon, K. Y. Guslienko, A. N. Slavin, D. V. Berkov, and N. L. Gorn, Phys. Rev. Lett. **88**, 047204 (2002).

[24] C. Kittel, Phys. Rev. **73**, 155 (1948).

[25] G. Gubbiotti and G. Carlotti (private communication).

[26] C. Bayer, S. O. Demokritov, B. Hillebrands, and A. N. Slavin, Appl. Phys. Lett. **82**, 607 (2003).